







Self-Reconfigurable Soft-Rigid Mobile Agent With Variable Stiffness and Adaptive Morphology

Luiza Labazanova , *Graduate Student Member, IEEE*, Shuang Peng , *Member, IEEE*, Liuming Qiu ,
Hoi-Yin Lee , Thrishantha Nanayakkara , *Senior Member, IEEE*,
and David Navarro-Alarcon , *Senior Member, IEEE*

Abstract—In this letter, we propose a novel design of a hybrid mobile robot with controllable stiffness and deformable shape. Compared to conventional mobile agents, our system can switch between rigid and compliant phases by solidifying or melting Field’s metal in its structure and, thus, alter the shape through the motion of its active components. In the soft state, the robot’s main body can bend into circular arcs, which enables it to conform to surrounding curved objects. This variable geometry of the robot creates new motion modes which cannot be described by standard (i.e., fixed geometry) models. To this end, we develop a unified mathematical model that captures the differential kinematics of both rigid and soft states. An optimised control strategy is further proposed to select the most appropriate phase states and motion modes needed to reach a target pose-shape configuration. The performance of our new method is validated with numerical simulations and experiments conducted on a prototype system.

Index Terms—Hybrid soft-rigid robots, shape control, variable stiffness, adaptive morphology, mobile agents.

I. INTRODUCTION

AUTONOMOUS mobile robots are one of the most prominent and well-established concepts in robotics. Self-contained design coupled with intelligent control systems allows mobile robots to perform a large variety of tasks. As such, they have been utilised in many industrial and service applications, including construction, conveyance, surface exploration, surveillance, entertainment, and others [1].

Manuscript received 13 October 2022; accepted 30 January 2023. Date of publication 2 February 2023; date of current version 9 February 2023. This letter was recommended for publication by Associate Editor C. Cao and Editor Y. Park upon evaluation of the reviewers’ comments. This work was supported in part by the Research Grants Council (RGC) of Hong Kong under grant 15212721 and in part by 2019/20 Belt and Road Scholarship (Research Postgraduate). (Corresponding author: David Navarro-Alarcon.)

Luiza Labazanova, Liuming Qiu, Hoi-Yin Lee, and David Navarro-Alarcon are with the Department of Mechanical Engineering, The Hong Kong Polytechnic University, Hung Hom, KLN, Hong Kong (e-mail: luiza.labazanova@connect.polyu.hk; valen.qiu@connect.polyu.hk; hoi-yin.lee@connect.polyu.hk; dna@iee.org).

Shuang Peng is with the Department of Aerospace and Mechanical Engineering, University of Southern California, Los Angeles 90007, CA USA (e-mail: shuangpe@usc.edu).

Thrishantha Nanayakkara is with the Dyson School of Design Engineering, Imperial College London, SW7 2DB South Kensington, U.K. (e-mail: t.nanayakkara@imperial.ac.uk).

The simulation source code is available at <https://github.com/Louashka/2sr-agent-simulation.git>.

This letter has supplementary downloadable material available at <https://doi.org/10.1109/LRA.2023.3241749>, provided by the authors.

Digital Object Identifier 10.1109/LRA.2023.3241749

Despite their advantages, mobile robots face considerable limitations common to most conventional robots. Constant morphology and rigid structures undermine their ability to adapt to surroundings, handle delicate objects and safely interact with humans. Moreover, such robots are limited in their functionality, thus, they are typically used for a narrow range of tasks. Different tasks require redesigning the robot’s structure. Soft robotics can solve these issues due to intrinsic versatility [2]; however, it complicates (and possibly limits) the system’s mobility and control since existing solutions operate via cumbersome actuators, their deformations are difficult to predict, and they lack high speed/force capacity [3].

In this work, we aim to improve the performance of mobile agents by leveraging paradigms of both conventional and soft robotics. We introduce a hybrid system with adaptive morphology that consists of a pair of wheeled locomotion units (LUs) connected by a variable-stiffness fibre (VSF). Sections with low-melting-point alloy (LMPA) within VSF serve as toggles between constant-shape and deformable modes. When the whole fibre is rigid, the robot acts as a conventional mobile robot. When LMPA is molten, VSF sections become soft; thus, a robot can reshape itself and conform to objects with various curved geometries [4], [5]. After the fibre solidification, its rigid structure maintains a modified shape. LUs carry power and electronics, which provides autonomy to a mobile system. The proposed adaptive morphology enables robots to be utilised in various applications (which contrasts with fixed geometry systems). For instance, they can serve as cleaning robots that collect different objects without additional grippers by deforming their body to perform manipulation tasks.

This new class of systems with adaptive morphology is primarily inspired by nature [6]. Biological species exploit similar variable shape principles to extend functionalities and facilitate locomotion in dynamic environments [7]. These benefits promoted research efforts in developing highly reconfigurable systems, including mobile robots [8], [9], [10]. For example, Kim et al. applied variable morphology to increase the locomotion capabilities of Whlegs [11] that allow a robot to traverse uneven surfaces. On flat surfaces, they are transformed into round wheels for high-speed motion. A similar idea lies behind robots that fold their whole body into a ball to roll on a plane [12]. Another solution was demonstrated by Nygaard et al. [13], in which a quadruped robot adjusts its legs length on the fly to fit into unstructured environments.

Several works have exploited variable morphology to create multi-functional devices such as self-reconfigurable systems [14] and foldable programmable matter with soft modules [15], [16], most of which typically lack mobility. Karimi

et al. [17] presented one of the pioneer studies in mobile hybrid self-reconfigurable robots. They developed a loop-shaped robot composed of rigid mobile units linked by a flexible membrane that becomes stiff by jamming its particles with an untethered vacuum system. This solution demonstrated promising results in locomotion and object handling, yet, its fixed number of active units may limit the system's scalability.

In this work, we present a new class of "Self-Reconfigurable Soft-Rigid Agent" (2SRA) that can be used either as a stand-alone mobile robot or as part of a multi-unit system. Self-reconfigurable refers to the system's capability to modify its morphology and also to its potential to be a part of a modular system. The original contribution of this work is twofold: (i) The development and experimental validation of a novel mobile robotic system with phase transition capabilities; (ii) The derivation of a mathematical model that captures the hybrid soft-rigid behaviour of the system and its locomotion properties.

The rest of this letter is organised as follows: Section II describes the robot's design, Section III derives the mathematical models, Section IV proposes the control strategy, Section V presents the experiments, and Section VI gives final conclusions.

II. MATERIALS AND METHODS

A. Variable-Stiffness Fibre

Variable-stiffness fibre (VSF) aims to alter the configuration and DoF of a 2SRA. For omnidirectional motion, the fibre must be stiff and capable of maintaining its shape. In a soft state, it should easily deform under the bending torque of its locomotion units. Therefore, the compliant features of the VSF are designed to have high flexibility and low elasticity.

Variable stiffness (VS) is an actively developing research field due to increasing demands in shape morphing technologies. Shape-memory alloys (SMA) have been widely employed for this purpose [18], e.g. Chenal et al. introduced a fabric with embedded SMA fibres, which undergo phase transitions when Joule heating is applied [19]. Another approach in VS is based on particle/layer jamming [20], such as in a hybrid self-reconfigurable robot [17] or hybrid robotic fingers [21]. We adopted a method presented by Tonazzini et al. [22] to create a VSF. Desired mechanical features are achieved by integrating a low melting point alloy (LMPA) and a Joule heater into the soft tube. Compared to SMAs, LMPAs have faster phase transitioning and lower power consumption [23] and they are easier to operate than jamming techniques. Among LMPAs, we chose Field's metal (composition by weight: 32.5% bismuth, 51% indium, and 16.5% tin). It is characterised by high absolute stiffness when solid (Young's modulus > 3 GPa), a low melting point around 62°C and low viscosity [24], [25].

Figs. 1(a), (b) show the VSF and its inner structure. The fibre is designed as a serial chain of variable-stiffness segments (VSS) with plastic links on both ends and Field's metal inside. This approach decreases fabrication complexity and increases robustness since separately fabricated modular segments can be easily replaced if they fail. For experiments, we fabricated a fibre with two VSS. Each plastic tube and segment are 30 mm and 40 mm long, respectively. Heaters are fabricated by coiling a magnet wire (0.1 mm in diam.) around the silicone rod (5 mm in diam.). A silicone tube (7 mm int. diam.; 8 mm ext. diam.) coaxial to the core encapsulates the whole device. The Field's metal is distributed between the tube and the rod. NTC thermistors (MF52AT) embedded in both segments measure the metal's

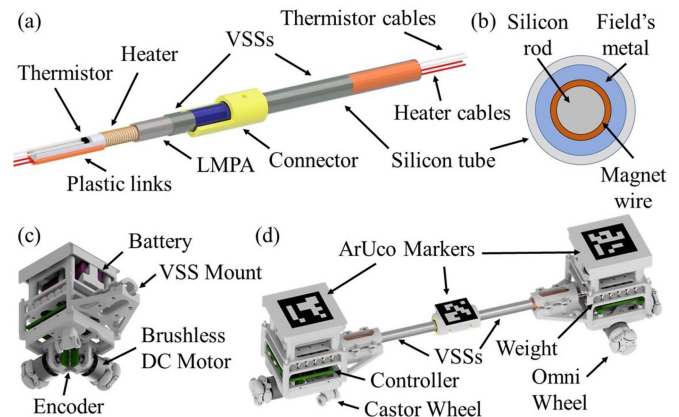


Fig. 1. Variable-stiffness fibre (VSF) with two segments: (a) Perspective view; (b) Cross-sectional view. (c) Locomotion unit (LU). (d) Assembled 2SRA.

temperature and provide feedback for stiffness control. Plastic links prevent metal leakage when it is in a liquid state and protect wires from external impact.

At room temperature, the fibre is rigid. A soft state is achieved by applying current to the coil and melting the alloy. It takes around 100 sec for the whole alloy layer to heat from 22°C to 62°C with 0.9 A (4.9–5.6 V) and 90 sec to completely solidify ($< 61^\circ\text{C}$).

B. Locomotion Units

We considered two main requirements when developing locomotion units:

- In a soft state, LUs must be able to actuate each end of the variable-stiffness fibre and bend segments into arcs with the desired curvature.
- In a rigid state, LUs must maintain a 3 DoF motion of a 2SRA on a plane with a given VSF configuration.

To meet these conditions, LUs are designed as a nonholonomic robot (Fig. 1(c)) with two omni-wheels (radius of 10 mm) placed perpendicular to each other on the adjacent unit sides. Their rotation in the same direction induces the unit's rotation, while the counter rotation promotes the linear motion along the diagonal between the wheels. A castor wheel in the opposite corner from the omni-wheels is used to stabilise the unit. Steel bars are placed inside the LU frame to increase the unit weight, which helps to improve the wheels' contact with the surface and to resist the restoring force produced by deformed VS fibre. When a VSF is rigid, units and fibre create a single agent, see Fig. 1(d). Four omni-wheels guarantee that the 2SR robot can translate freely on a plane even if the opposite wheels are not parallel.

A custom controller board with STM32 microcontroller operates brushless DC motors to drive wheels and actuates a VSS. AS5600 encoders control the motors' speed and a Li-ion battery (3.7 V, 1000 mAh) boosted to 9.6 V powers the system. PWM output with analogue signal captured from a thermistor as feedback is used to control heaters. A wireless serial board provides communication with the server. All electronics are enclosed in a 3d-printed plastic frame ($46 \times 46 \times 78$ mm).

III. MODELLING

Integrating entirely different natures of rigid and soft bodies in one robot significantly expands its capabilities; however, it

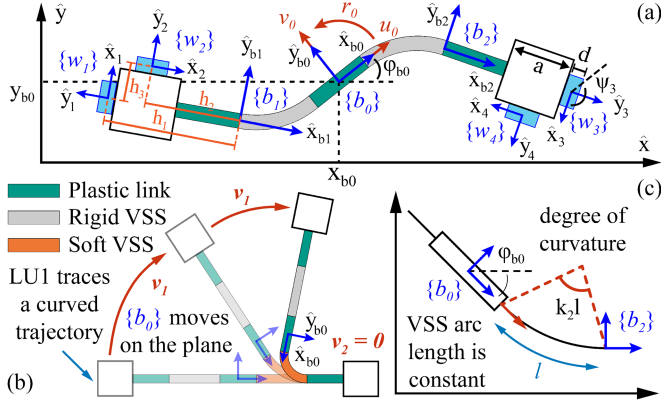


Fig. 2. (a) Schematic representation of a 2SR robot with two variable-stiffness segments (VSS). (b) Reconfiguration of a 2SR robot when one of its segments is soft. The motion of a locomotion unit (LU) adjacent to the rigid segment results in a displacement of the body frame $\{b_0\}$. (c) Geometrical features of constant curvature approximation for a VSS arc.

becomes challenging to derive a unified model. This section introduces a hybrid control strategy that combines 2SRA configurations in both rigid and soft states. Switching between states is considered a Boolean operation; thus, the heating and cooling processes are not included in the model. This model is adapted for a robot with two variable-stiffness segments, but it can be customised for any fibre design.

A. Analysis of the System's Hybrid Kinematics

Due to the 2SRA dual nature, we conduct kinematic analysis separately for rigid and soft states and then combine those pieces in one model. To simplify calculations, we assume fibre segments are inextensible and strictly bend into circular arcs with constant curvature. Also, we consider that motion of the units in the soft state is independent of each other.

Fig. 2(b) demonstrates a scenario when one VSS is soft, and a 2SR agent can change its shape. LUs can move together or one at a time. According to schematics in Fig. 2(a), omni-wheels indexing starts from the left side wheel of LU1 and follows clockwise. Robot's body frame $\{b_0\}$ is attached to the middle point of the plastic connector. Two other frames $\{b_1\}$ and $\{b_2\}$ are attached to VSS ends. The angles between these frames and the wheel frames $\{w_i\}$, $i \in [1..4]$, are $\beta_1 = \frac{\pi}{2}$, $\beta_2 = 0$, $\beta_3 = -\frac{\pi}{2}$, and $\beta_4 = \pi$ with the former two wheels associated with $\{b_1\}$ and the latter two with $\{b_2\}$.

The biggest contribution to the fibre bending is provided by the lateral wheels ($\{w_1\}$, $\{w_3\}$). Velocities tangential to bending trajectory correspond to the maximum torque and thus are energy efficient. On the other hand, the motion of the other wheels promotes free rod deformation, which is challenging to perform since it requires high forces that are not feasible with the current design. Therefore, we neglect these wheels during VSS bending and keep their rotational speed at zero: $\omega_1 = \frac{1}{\rho_\omega} v_1$, $\omega_3 = -\frac{1}{\rho_\omega} v_2$, and $\omega_2 = \omega_4 = 0$, where ω_i is the angular velocity of the i^{th} wheel; v_1 and v_2 are velocities of the first and second units traversing some curved path; and ρ_ω is the wheel radius. In matrix representation, this relationship is defined as $\omega = \mathbf{V}^s \mathbf{v}^s$:

$$\mathbf{V}^s = \frac{1}{\rho_\omega} \begin{bmatrix} 1 & 0 & 0 & 0 \\ 0 & 0 & -1 & 0 \end{bmatrix}^\top, \quad (1)$$

where \mathbf{V}^s is the wheels configuration matrix when 2SR agent is in a soft state; $\omega = [\omega_1 \dots \omega_4]^\top$ and $\mathbf{v}^s = [v_1, v_2]^\top$.

In the second scenario, the fibre is rigid, and 2SRA behaves like a conventional mobile robot. A remarkable feature of this state is that omnidirectional motion can be achieved at any fibre configuration since the relative position of omni-wheels ensures three degrees of freedom. For omnidirectional robots with four wheels, a generalised wheel model is defined as:

$$\omega_i = \begin{bmatrix} \frac{1}{\rho_i} & \frac{t\gamma_i}{\rho_i} \end{bmatrix} \begin{bmatrix} c\psi_i & s\psi_i \\ -s\psi_i & c\psi_i \end{bmatrix} \begin{bmatrix} 1 & 0 & -b_0 y_{w_i} \\ 0 & 1 & b_0 x_{w_i} \end{bmatrix} \begin{bmatrix} u_0 \\ v_0 \\ r_0 \end{bmatrix}, \quad (2)$$

where ω_i is the i^{th} wheel velocity; ρ_i is the radius of the i^{th} wheel; γ_i is an angle between the roller axis (rotation axis of small passive discs) and the \hat{x}_i axis of the wheel frame $\{w_i\}$; ψ_i is an angle between the body frame $\{b_0\}$ and $\{w_i\}$; $b_0 x_{w_i}$ and $b_0 y_{w_i}$ are position coordinates of $\{w_i\}$ w.r.t. $\{b_0\}$; u_0 , v_0 , and r_0 are forward, lateral, and angular robot velocities. By $s\psi_i$ and $c\psi_i$ we denote sine and cosine of the angle ψ_i . Since all omni-wheels have the same radius ρ_ω , and their roller axes coincide with the \hat{x} axes that is $\gamma_i = 0 \forall i \in [1, \dots, 4]$, (2) can be rewritten in the form of $\omega = \mathbf{V}^r \mathbf{v}^r$:

$$\mathbf{V}_i^r = [c\psi_i \quad s\psi_i \quad b_0 x_{w_i} s\psi_i - b_0 y_{w_i} c\psi_i] / \rho_\omega, \quad (3)$$

where \mathbf{V}_i^r is the i^{th} row of a configuration matrix \mathbf{V}^r when a 2SR agent is in a rigid state and $\mathbf{v}^r = [u_0, v_0, r_0]^\top$. Variables ψ_i , $b_0 x_{w_i}$ and $b_0 y_{w_i}$ depend on the fibre shape and thus to be recalculated accordingly. Analysis of the relationship between them and segments curvatures are given in the next section.

Combination of both approaches in $\omega = \mathbf{V} \mathbf{v}$ gives a vector of input velocities $\mathbf{v} = (\mathbf{v}^s, \mathbf{v}^r)$, in which either v_1 and v_2 or u_0 , v_0 and r_0 are non-zero. This condition depends on the segments' stiffness. To represent the stiffness of the j^{th} VSS, we introduce a boolean variable ς_j , which is equal to zero when the segment is rigid and one when it is soft. Thus, we obtain a unified wheels configuration matrix:

$$\mathbf{V}_i = \frac{1}{\rho_\omega} [\sigma \wedge (i=1) \quad -\sigma \wedge (i=3) \quad \bar{\sigma} c\psi_i \quad \bar{\sigma} s\psi_i \quad \bar{\sigma} \tau_i], \quad (4)$$

where $\sigma = \varsigma_1 \vee \varsigma_2$ and $\tau_i = b_0 x_{w_i} s\psi_i - b_0 y_{w_i} c\psi_i$; \vee and \wedge are logical disjunction and conjunction, respectively, and notation \bar{A} is a logical negation.

B. Wheels Configuration

For the robots with fixed geometry, matrix \mathbf{V} from (4) is constant. However, a 2SRA is capable of changing its shape, which entails the variation of the wheels' coordinates relative to the body frame. Therefore, the issue to address is determination of the i^{th} wheel coordinates ${}^{b_0} \mathbf{q}_{w_i} = [{}^{b_0} x_{w_i}, {}^{b_0} y_{w_i}]^\top$ and ψ_i for any robot configuration. Coordinates of the wheels with reference to the associated fibre ends are always constant and can be expressed as:

$${}^{b_0} \mathbf{Q}_w = \begin{bmatrix} -h_1 & -h_2 & h_1 & h_2 \\ 0 & h_3 & 0 & -h_3 \end{bmatrix}, \quad (5)$$

where $h_1 = \frac{2l_1 + 2a + d}{2}$, $h_2 = \frac{2l_1 + a}{2}$, and $h_3 = \frac{a + d}{2}$; a is the block side length, d is the wheel thickness, and l_1 is the length of the plastic links at the ends of the fibre. Positional coordinates w. r. t. the robot body frame $\{b_0\}$ are further derived through a

homogeneous transformation

$$[{}^{b_0}\mathbf{q}_{w_i}^\top \ 1]^\top = {}^{b_0}\mathbf{T}_{b_j} [{}^{b_j}\mathbf{q}_{w_i}^\top \ 1]^\top, \quad (6)$$

where ${}^{b_j}\mathbf{q}_{w_i}$ is the i^{th} column of ${}^{b_j}\mathbf{Q}_w$ and $\{b_j\}$ denotes the fibre end associated to the i^{th} wheel. Thus, the solution to the problem is reduced to mapping frames $\{b_j\}$ to the frame $\{b_0\}$, which depends on the segment arc curve.

We assume that VSS bends into a circular arc with constant curvature; thus, the position of any point on the segment arc can be defined as $x_j(p) = x_j(0) + (s\theta_j(p) - s\theta_j(0))/\kappa_j$ and $y_j(p) = y_j(0) - (c\theta_j(p) - c\theta_j(0))/\kappa_j$, where j denotes the j^{th} segment, p_j is the position along the segment length, κ_j is the signed curvature, and $\theta_j(p) = \theta_j(0) + \kappa_j p$ is the arc point's orientation. Since all segments are inextensible, and their length l remains constant during robot deformation, we derive a transformation matrix from the above equations as follows:

$${}^{b_0}\mathbf{T}_{b_j} = \begin{bmatrix} c\alpha_j & (-1)^{j-1}s\alpha_j & (-1)^j \left(\frac{l_0}{2} + \frac{s\alpha_j}{\kappa_j} \right) \\ (-1)^j s\alpha_j & c\alpha_j & \frac{1-c\alpha_j}{\kappa_j} \\ 0 & 0 & 1 \end{bmatrix}, \quad (7)$$

where l_0 is the length of the middle link, j is the segment index, and $\alpha_j = \kappa_j l$ is the degree of curvature, see Fig. 2(c). Accordingly, we find an orientation of the wheel frame:

$$\psi_i = \phi_{b_0} + (-1)^j \alpha_j + \beta_i, \quad (8)$$

where ϕ_{b_0} is orientation of $\{b_0\}$ w.r.t. to the global frame.

C. LU Paths Estimation

The further analysis involves estimating paths traced by LUs when either of the VS segments is soft. We consider segment deformation as an arc of a constant length and curvature. Assuming that VSS can bend into a full circle (though it is not feasible with a real robot), we can see that its tip traces a curve that resembles a piece of a logarithmic spiral, see Fig. 3. Matlab was used to fit the spiral to the segment arc points according to the following curve representation:

$$\rho = ae^{b\theta}, \quad x = \rho c\theta, \quad y = \rho s\theta, \quad (9)$$

where θ is the spiral angle from x -axis; ρ is the spiral radius at an angle θ ; and a and b are arbitrary constants.

We distinguish three general motion modes at a soft state: one segment is soft, and the adjacent unit is moving (Case 1); one segment is soft, and the opposite unit is moving (Case 2); both segments are soft (Case 3). We denote a rigid motion mode as Case 0. Graphs in Fig. 3 demonstrate that Cases 1-3 correspond to differently shaped logarithmic spirals; therefore, we first analyze each spiral and then combine their features into a unified kinematic model.

1) *Case 1. Soft-Rigid*: The first considered case ($\varsigma_1 = 0, \varsigma_2 = 1, v_1 = 0$, and $v_2 \neq 0$) is illustrated in Fig. 3(a, b). By varying the fibre length l from 1 to 100 cm in Matlab we determined that spiral parameter b , the relationship between l and a , and the relationship between l and spiral centre $\{c\}$ are constant. Parameters of all three spirals are listed in Table I. Values of the spirals' centres are not used further since they have been eliminated during calculations; nonetheless, they are provided for complete information on spirals. The sign of b depends on curvature κ ; if it is positive, then b is negative and vice versa. In a 2SRA, the change of curvature κ linearly depends on the change

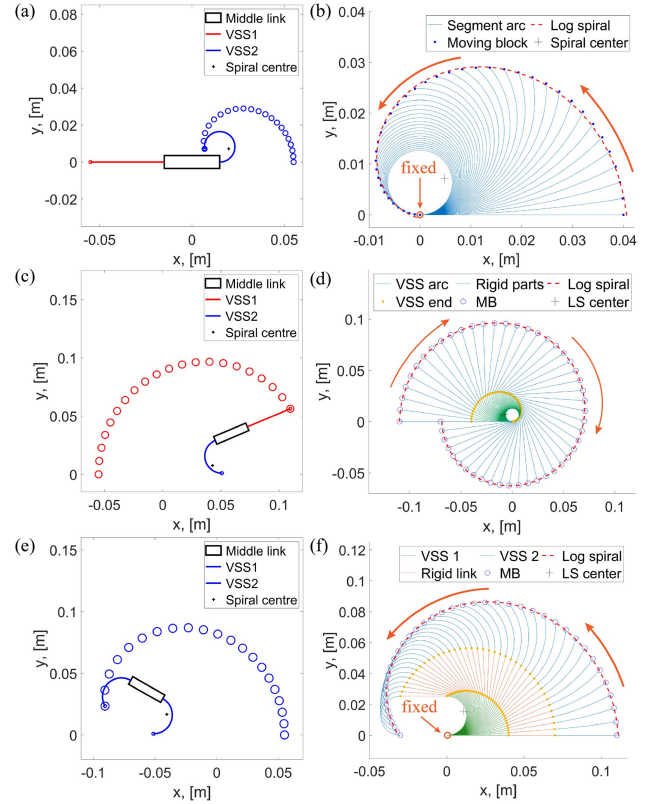


Fig. 3. Shape deformation of a 2SR robot and corresponding logarithmic spirals when: (a), (b) one soft VSS is bent by an adjacent LU (Case 1); (c), (d) one soft VSS is bent by the opposite LU (Case 2); (e), (f) both segments are soft (Case 3).

TABLE I
PARAMETERS OF LOGARITHMIC SPIRALS

Spiral	a/l	b	c_x/l	c_y/l
I	2.325	± 0.3165	-0.1223	0.1782
II	3.3041	± 0.083	0.1988	0.1640
III	2.4471	± 0.2229	-0.2722	0.3949

of θ ; therefore, we approximate their relationship by mapping their ranges $-\pi/3 \leq \theta_1 \leq 7\pi/3$ and $-2\pi/l \leq \kappa_1 \leq 2\pi/l$:

$$\kappa_j = 3(\theta_1 - \pi)/(2l). \quad (10)$$

2) *Case 2. Rigid-Soft*: The motion of the unit adjacent to a rigid VSS ($\varsigma_1 = 0, \varsigma_2 = 1, v_1 \neq 0$, and $v_2 = 0$) resembles a logarithmic spiral even more clearly, see Fig. 3(c, d). Here, the absolute value of b is sensitive to the ratio of the lengths of soft and rigid items. We applied fibre custom values used during fabrication. Relationship between spiral angle and segment curvature with given ranges $-\pi \leq \theta_2 \leq 3\pi$ and $-2\pi/l \leq \kappa_2 \leq 2\pi/l$ is:

$$\kappa_j = (\theta_2 - \pi)/l. \quad (11)$$

3) *Case 3. Soft-Soft*: The last case involves a 2SRA deformation with both segments being soft ($\varsigma_1 = 1, \varsigma_2 = 1, v_1 = 0$, and $v_2 \neq 0$), see Fig. 3(e). Bending spreads uniformly along the fibre; thus, segment curvatures change equally. According to the corresponding logarithmic spiral (Fig. 3(f)), units meet each other faster since segments' curvatures are summed up. Therefore, we limit each VSS to bend into a half-circle so that

$$-\frac{\pi}{3} \leq \theta_3 \leq \frac{7\pi}{3} \text{ and } -\frac{\pi}{l} \leq \kappa_3 \leq \frac{\pi}{l}: \quad (12)$$

$$\kappa_j = 3(\theta_3 - \pi)/(4l).$$

D. Unified Jacobian Matrix

Configuration of a 2SR agent is fully defined by five generalised coordinates $\mathbf{q} = [x_{b_0}, y_{b_0}, \phi_{b_0}, \kappa_1, \kappa_2]^\top$, where x_{b_0}, y_{b_0} and ϕ_{b_0} are position coordinates and orientation of the body frame $\{b_0\}$ w.r.t. to the global frame, and κ_j is the curvature of the j^{th} VSS. Then, the forward kinematics of a 2SR agent is described as:

$$\dot{\mathbf{q}} = \mathbf{J}\mathbf{v}, \quad (13)$$

where $\mathbf{v} = \mathbf{V}^\dagger \boldsymbol{\omega}$ and \mathbf{J} is a Jacobian matrix. \mathbf{V}^\dagger is the Moore-Penrose pseudo inverse of a configuration matrix \mathbf{V} from (4).

In order to find a unified Jacobian matrix, we apply a state-centric approach as in the previous sections. We divide a Jacobian matrix into two parts: $\mathbf{J} = [\mathbf{J}^s, \mathbf{J}^r] \in \mathbb{R}^{5 \times 5}$, where \mathbf{J}^s and \mathbf{J}^r are Jacobian matrices that correspond to the soft and rigid states, respectively. $\mathbf{J}^r \in \mathbb{R}^{5 \times 3}$ consists of a rotation matrix $R_z(\phi_{b_0})$ and two zero rows. The matrix $\mathbf{J}^s \in \mathbb{R}^{5 \times 2}$ maps velocity input commands into \mathbf{q} coordinates according to the logarithmic spirals traced by locomotion units.

VSS curvature can be determined through the spiral angle θ , which rate of change is proportional to the speed of the object tracing the spiral: $\dot{\theta} = \frac{1}{\rho(\theta)}v$. By substituting the angle θ_k by the curvature equations from (10)–(12), we receive a relationship between curvature change and the LU velocity v :

$$\dot{\kappa}_j = \frac{m_k}{l\rho_k(\kappa_j)}v, \quad (14)$$

where $k = [1..3]$ denotes the serial number of the spiral case, $\mathbf{m} = [\frac{3}{2}, 1, \frac{3}{4}]^\top$ is the set of constants that correspond to the k^{th} spiral, and $\rho_k(\kappa_j) = a_k \exp(b_k(\frac{\alpha_j}{m_k} + \pi))$. Further, we denote the proportionality coefficient as $K_{k,j} = \frac{m_k}{l\rho_k(\kappa_j)}$.

The next step is to find the body frame coordinates. In Case 1, a VSF connector is stationary; thus, $\dot{x}_{b_0} = \dot{y}_{b_0} = \dot{\phi}_{b_0} = 0$. Cases 2 and 3 involve the motion of the middle link with a body frame attached to it. Its orientation is equal to the orientation of the tangent at the VSS arc point closest to the body frame, which is calculated as $\phi_{b_0} = \phi_{b_j} \pm \alpha_j$, see Fig. 2(c). It implies that the rate of change of the robot orientation linearly depends on the rate of curvature change:

$$\dot{\phi}_{b_0} = \frac{m_k}{\rho_k(\kappa_j)}v. \quad (15)$$

We denote the proportionality coefficient as $\Phi_{k,j} = \frac{m_j}{\rho_j(\kappa_j)}$.

Schematic representation of 2SRA geometry during shape deformation in Fig. 4(a) demonstrates the relationship between fibre frames and logarithmic spiral from Case 1. The connection point G between VSS and the middle link lies on the spiral and its position w.r.t. the spiral centre $\{c\}$ is found according to (9). Since the position of the point F attached to the body frame origin is fixed relative to G , we find:

$${}^c F = \left[\frac{l_0 c \alpha_j}{2} + \rho_1(\kappa_j) c \frac{\alpha_j}{m_1} \quad \frac{l_0 s \alpha_j}{2} + \rho_1(\kappa_j) s \frac{\alpha_j}{m_1} \right]^\top. \quad (16)$$

We can express frames $\{b_j\}$ through $\{b_0\}$ and $\{c\}$. Thus, position coordinates of the point F with respect to the global frame $\{o\}$ can be expressed as a series of kinematic transformations as:

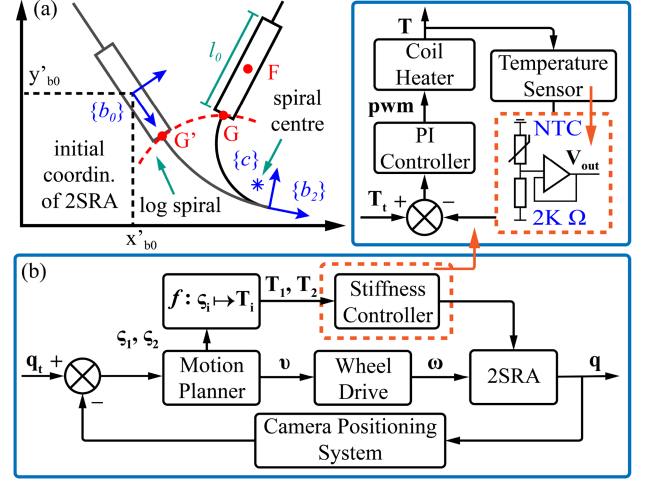


Fig. 4. (a) The relationship between 2SR robot coordinates and the geometry of the logarithmic spiral I. (b) 2SRA control strategy.

${}^o F = {}^o T_{b_0} {}^{b_0} T_{b_j} {}^{b_j} T_c {}^c F$, which partial derivatives with respect to κ_j provides the relationship between the rate of change of the robot position coordinates, the LUs velocities v_j , and their logarithmic trajectories:

$$x_{b_0} = \frac{\partial {}^o F_x}{\partial \kappa_j} \frac{\partial \kappa_j}{\partial t}, \quad y_{b_0} = \frac{\partial {}^o F_y}{\partial \kappa_j} \frac{\partial \kappa_j}{\partial t}. \quad (17)$$

Denoting $\Delta_{k,j} = \frac{\partial {}^o F}{\partial \kappa_j} K_{k,j}$, $\xi_1 = \overline{\varsigma_1} \varsigma_2$, $\xi_2 = \varsigma_1 \overline{\varsigma_2}$, $\xi_3 = \varsigma_1 \varsigma_2$, and $\mathbf{C}_{k_1,j}^{k_2,k_3} = [\Delta_{k_1,j}^\top, (-1)^{j+1} \Phi_{k_1,j}, K_{k_2,1}, K_{k_3,2}]^\top$ we get:

$$\mathbf{J}^s = \begin{bmatrix} \xi_1 & -\xi_1 & \xi_2 & \xi_1 \\ \xi_2 & \xi_2 & \xi_2 & \xi_1 \end{bmatrix}^\top \circ \begin{bmatrix} \mathbf{C}_{2,2}^{1,2} \\ \mathbf{C}_{2,1}^{2,1} \end{bmatrix}^\top + s_3 \begin{bmatrix} \mathbf{C}_{3,2}^{3,3} \\ \mathbf{C}_{3,1}^{3,3} \end{bmatrix}^\top, \quad (18)$$

where \circ denotes the element-wise matrix multiplication.

IV. CONTROLLER DESIGN

A distinctive feature of a 2SRA is the real-time transition between rigid and soft states. This quality is exploited by a single-agent control strategy designed for scenarios with no obstacles between the initial and target configurations. A block diagram in Fig. 4(b) shows that the proposed algorithm comprises three main components: Motion Planner, Wheel Drive, and Stiffness Controller.

At any given moment, a 2SR agent can switch between four locomotion modes. A Motion Planner aims to select a sequence of these modes most suitable for the given task. Possible configurations of the VSF are defined by a set $\varsigma = [[0, 0], [0, 1], [1, 0], [1, 1]]^\top$. Each iteration of the trajectory formation calculates unified Jacobian matrices corresponding to the elements of ς . They are further supplied to the inverse kinematics equations. Among the Euclidean distances between the target configuration q_t and the set of potential configurations $q^*[i]$, we choose the smallest one. However, in this approach, we might get solutions involving frequent changes in segments' stiffness. Phase transitions of the Field's metal take time; therefore, these situations are highly undesirable. We avoid this issue by maintaining established stiffness values as long as the robot drives towards the target. Once an intermediate configuration stops

Algorithm 1: 2SR Agent Motion Planner

Input: Initial configuration q_0 , target configuration q_t
Output: List of stiffness values Ω , list of velocities \mathcal{V}

- 1 $\zeta \leftarrow$ set of possible VSF stiffness values
- 2 $\Omega, \mathcal{V} \leftarrow$ empty lists
- 3 **while** $\|q_t - q\| > 0$ **do**
- 4 **for** $i = 1$ **to** 4 **do**
- 5 $J \leftarrow$ hybridJacobian($q_0, q, \zeta[i]$)
- 6 $v[i] \leftarrow J^{-1}\lambda(q_t - q)$ // λ - feedback gain
- 7 $\dot{q} \leftarrow Jv[i]$
- 8 $q^*[i] \leftarrow q + \dot{q}dt$
- 9 $\Delta q^* \leftarrow \|q_t - q^*\|$
- 10 $i^* \leftarrow \arg \min_i \Delta q^*$
- 11 **if** $i^* \neq i_{prev}$ **then**
- 12 **if** $\|q - q^*[i_{prev}]\| > 0$ **then**
- 13 $i^* \leftarrow i_{prev}$
- 14 $q \leftarrow q^*[i^*]$
- 15 Add $\zeta[i^*]$ to Ω ; Add $v[i^*]$ to \mathcal{V}

updating, the locomotion mode is changed to the appropriate option. The Motion Planner pseudocode is given in Algorithm 1.

A sequence of 2SRA velocities returned by the Motion Planner is converted into the wheels' velocities by Wheel Drive defined by the model derived in (1)–(8). A sequence of VSSs' stiffness values is mapped to the temperature values that are required to either melt the Field's metal (taken with margin) for the soft state or to cool it down for the rigid state: $T_j(\zeta_j) = 65^\circ$ if $\zeta_j = 1$ else 25° .

The stiffness controller maintains the melting point when it is requested and notifies the main controller when the required temperature has been achieved. A PI controller regulates the current applied to the heater and receives feedback from the sensor. Temperature is measured via an NTC MF52AT thermistor. We constrain its operating range to $[0^\circ \dots 85^\circ]$ to avoid overheating the copper coil. This range is mapped to voltage output $[1.1, \dots, 3.3]$ V.

V. RESULTS

A. Experimental Setup and Simulation

Fig. 5(a) shows an experimental set-up, which involved a 2SR agent with three Aruco markers attached to the locomotion units and the VSF connector, RealSense camera, thermal camera and a server. The coordinates of the VSF marker corresponded to the position coordinates of the robot b_0 frame, while the LU markers were used to estimate the segments' curvature with the assumption that it is constant along the arc. The agent's motion was kept within the tracked boundaries defined by Aruco markers, which, with the other markers, were captured by the RealSense camera. A thermal camera was used to analyse VSS temperature.

Before conducting experiments, we passed our model through a simulator deployed in a Python environment. Plots in Fig. 5(b) compare the change of error $\Delta q = \|q_t - q\|$ in trajectories generated by Forward Kinematics (FK) and Motion Planner (MP). First, we run FK with a random initial configuration and constant velocity and VSF stiffness, which yields a linear increment of the robot's coordinates. The last state in FK path is supplied

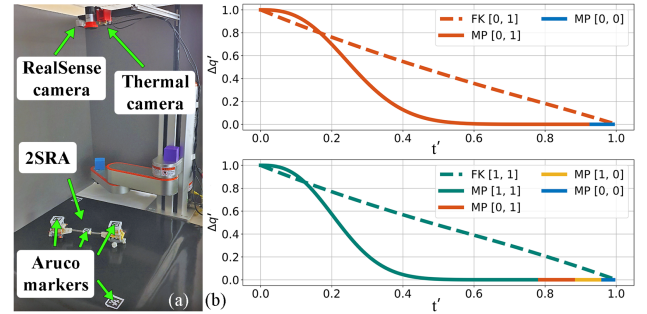


Fig. 5. (a) Experimental setup. (b) Comparison of error minimization in Forward Kinematics (FK) and Motion Planner (MP) trajectories. Time t and error Δq are normalised with min-max scaling: $t' = (t - t_{\min}) / (t_{\max} - t_{\min})$ and $\Delta q' = (\Delta q - \Delta q_{\min}) / (\Delta q_{\max} - \Delta q_{\min})$. The last section of the MP graph shows that a 2SR agent sometimes has to switch motion modes to fit into the target: one time (top figure); three times (bottom figure).

as a target configuration to the Motion Planner, which is an asymptotically stable control algorithm; therefore, Δq decreases exponentially. Due to different scales of positional and curvature coordinates, the latter sometimes approaches the desired values faster. Then, 2SRA has to switch stiffness and motion modes to fit the target completely. Within 100 simulations, a robot exploited at most four motion modes, in which the last one was always Case 0.

B. Curvature Estimation

The proposed hybrid model uses a constant curvature (CC) approximation for VSS. We evaluated the actual curvature distribution along the segment to validate a CC assumption. One VSS was kept rigid while its adjacent LU was fixed on the plane. Another segment was gradually bent in both directions with a degree of curvature varying from $[-\pi \dots \pi]$. The hot area of the soft VSS was extracted from the images captured by the thermal camera, see Fig. 6(a) and further processed. The binary image in Fig. 6(b) shows the segment contours and median curve constructed via the OpenCV library. Fig. 6(c) compares the estimated, smoothed and approximated segment arcs. Finally, calculating the gradient in each point of the smoothed median curve returned a corresponding array of curvatures. Test trials were repeated five times.

Results of the experiment presented in Fig. 7(a) show that the mean curvature (MC) of the VSS median curve and the corresponding CC calculated from the pose of Aruco markers are quite similar at the small values and more diverse at larger bending. The overall mean square error between CC and MC is 9.09 m^{-1} , and the average standard deviation of curvature distribution along the segment is 14.39 m^{-1} . Curvatures in the range of $0 - 15 \text{ m}^{-1}$ are comparatively small regarding the length of the segments, hence, the CC assumption provides an adequate representation of VSS bending.

C. Pose-Shape Formation

Pose-Shape Formation tasks involve reaching a given target with simultaneous motion on a plane and bending the segments. We implemented a control strategy provided in Section IV and conducted five experiments with different initial and target configurations. They were obtained by manually deforming the robot, placing it in the desired spot and measuring the corresponding configuration through a RealSense camera. The same

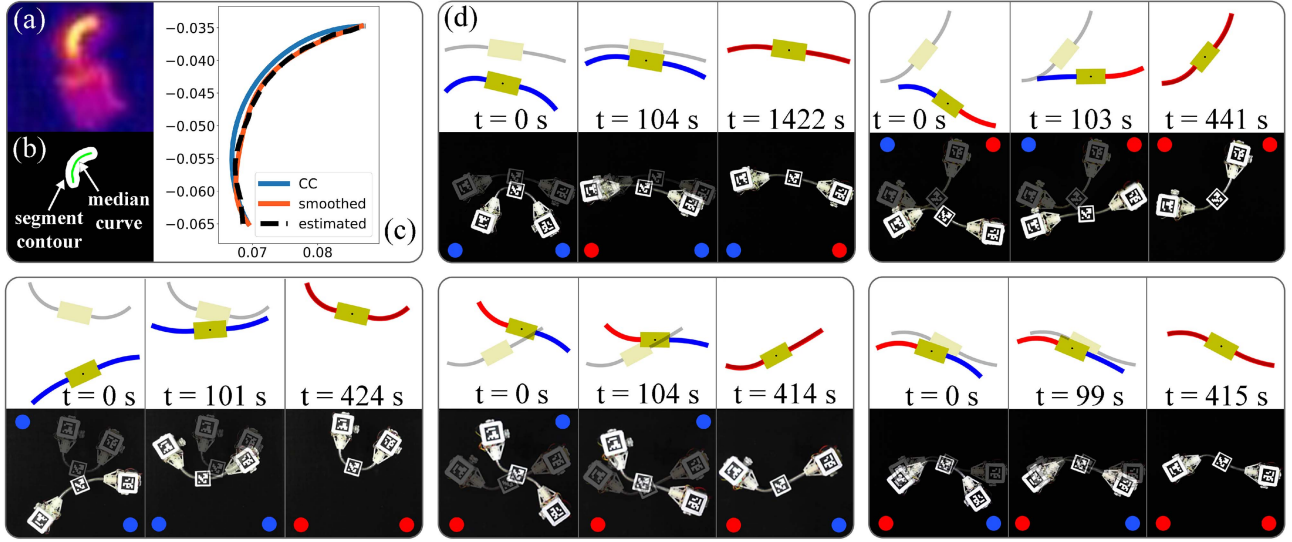


Fig. 6. (a) Thermal image of a soft VSS. The bright-coloured area shows the high-temperature zone of the molten LMPA inside the segment's shell. (b) Contours and a median curve of the bent segment extracted from a thermal image. (c) Comparison of the median curve, its smoothed version and the approximated curve with constant curvature. (d) Five scenarios of the pose-shape formation when a robot has a task to reach a target configuration. The top row shows the 2SRA simulation, and the bottom row is the real-case motion. Blue colour represents a soft segment while a rigid segment is red. A faded image shows a target; the bright one is the current configuration. The first case takes more time because the agent switched stiffness more than one time.

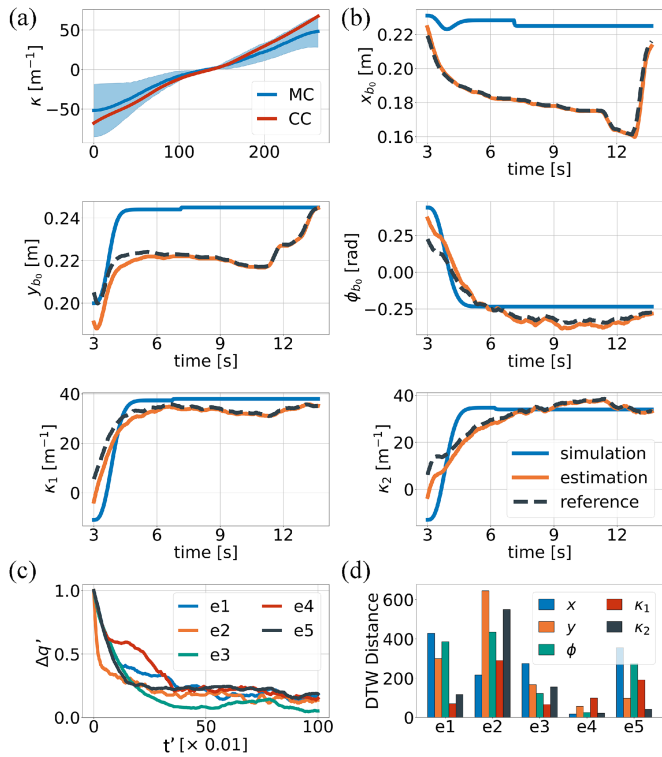


Fig. 7. (a) Comparison of the VSS constant curvature (CC) approximation and mean curvature (MC) of the segment arc extracted from thermal images. The solid-coloured area demonstrates curvature distribution along the segment arc. (b) Comparison of the configuration trajectories obtained during the Pose-Shape Formation experiment (third case) and the corresponding simulation. Reference is the configuration returned by a Motion Planner and further supplied to the robot; the Estimated value is the configuration measured via camera and Aruco markers. (c) Minimization of the normalised error $\Delta q'$ during the task execution. (d) Quantified difference (DTW distance) between the configuration trajectories from the Pose-Shape Formation experiments and corresponding simulations.

inputs were tested in the simulator and later compared to the real-case scenarios.

All trials differ in motion cases and duration. Fig. 6(d) demonstrates the execution process of the tasks and corresponding simulations. In both scenarios, a 2SRA shows a similar movement pattern. At each moment of the robot's motion, we assessed a reference configuration selected by a Motion Planner and an estimated configuration measured through the camera. The comparison of the trajectories obtained during the 3rd experiment and its simulation is provided in Fig. 7(b). It was observed that sometimes lateral wheels slip when a 2SRA is deforming. Soft VSF slacks and tilts LUs, because of which lateral wheels lose solid contact with a surface. It causes some deviations from a simulated trajectory, which is more obvious in positional coordinates since their scale is much smaller compared to curvature. A potential solution might be increasing the number or weight of steel bars within LUs. Fig. 7(c) shows how the robot approaches the target. We stopped the motion as soon as $\Delta q'$ hits the given thresholds (< 0.01 for $\langle x_{b_0}, y_{b_0} \rangle$, < 4 for $\langle \kappa_1, \kappa_2 \rangle$) to avoid frequent stiffness alternation. Bar plot in Fig. 7(d) summarises the experimental results by calculating the Dynamic Time Warping (DTW) distance between the simulated and experimental trajectories. These errors are not significant, and a 2SR robot is capable of approaching the target under the proposed hybrid model.

D. Applications

The adaptive nature of a 2SRA makes it useful for a large variety of tasks. Its main advantage is the ability to conform to curved objects. In Fig. 8(a), a 2SR agent approaches a cylindrical object and bends one of its segments until it fits a given shape. Another example in Fig. 8(b) shows object manipulation. Execution of this task runs as follows: a 2SRA approaches the target, turns both segments soft, grasps the cube and goes back

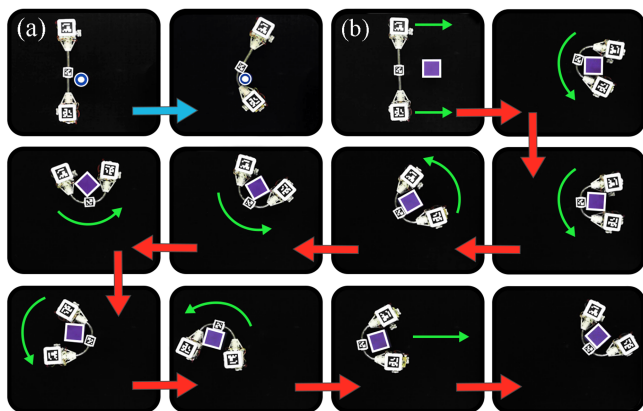


Fig. 8. 2SR agent performing objects handling tasks: (a) conforming to an object with a cylindrical shape. (b) gripping and moving a cube on the plane. The video is available at https://youtu.be/zL0pZ_69aC4.

TABLE II
COMPARISON OF A 2SR AGENT WITH THE STATE OF ART

	[10]	[12]	[17]	2SRA
Shape shifting	✓	✓	✓	✓
Conforming to surroundings	✓	✗	✓	✓
Variable stiffness	✗	✗	✓	✓
Variable motion modes	✓	✓	✗	✓
High-speed locomotion	✓	✓	✗	✓
Untethered actuation	✗	✓	✓	✓

to a rigid state. After VSF solidification, a robot moves freely on a plane while handling the cube.

These are a few examples of how a 2SRA can be used. Potential applications are not limited to any specific area since, unlike other mobile robots, a 2SR agent aims to combine the best features of conventional and soft robotics. A comparison of a 2SRA with the state of the art is given in Table II.

VI. CONCLUSION

This letter presented a new type of mobile robot that can behave either as a conventional rigid agent or as a hybrid deformable robot. It consists of two locomotion units connected by a serial variable-stiffness fibre. VSF enables transitions between rigid and soft states. LUs carry power and electronics, perform 2 d motion and actuate the fibre. A unified hybrid model is developed to describe the behaviour of a 2SR agent in both states. Shape deformation and LUs motion when VSF segments are soft are described based on approximated logarithmic spirals traced by the units. The proposed design and model were tested in simulation and physical experiments.

Experiments in reaching the target and handling the objects demonstrated promising results. A 2SRA benefits from the ability to adapt to the surroundings and chooses the most appropriate stiffness and motion mode to execute the task. Our future plans involve developing a modular system of multiple agents and reducing the VSF phase transitioning time, which will make 2SR robots suitable for applications where fast response is needed.

REFERENCES

- [1] F. Rubio, F. Valero, and C. Llopis-Albert, "A review of mobile robots: Concepts, methods, theoretical framework, and applications," *Int. J. Adv. Robot. Syst.*, vol. 16, 2019, Art. no. 1729881419839596.
- [2] S. Kim, C. Laschi, and B. Trimmer, "Soft robotics: A bioinspired evolution in robotics," *Trends Biotechnol.*, vol. 31, pp. 287–294, 2013.
- [3] C. Zhang, P. Zhu, Y. Lin, Z. Jiao, and J. Zou, "Modular soft robotics: Modular units, connection mechanisms, and applications," *Adv. Intell. Syst.*, vol. 2, 2020, Art. no. 1900166.
- [4] W. Shan, T. Lu, and C. Majidi, "Soft-matter composites with electrically tunable elastic rigidity," *Smart Mater. Struct.*, vol. 22, 2013, Art. no. 085005.
- [5] D. Navarro-Alarcon and Y.-H. Liu, "Fourier-based shape servoing: A new feedback method to actively deform soft objects into desired 2-D image contours," *IEEE Trans. Robot.*, vol. 34, no. 1, pp. 272–279, Feb. 2018.
- [6] R. Pfeifer, M. Lungarella, and F. Iida, "Self-organization, embodiment, and biologically inspired robotics," *Science*, vol. 318, pp. 1088–1093, 2007.
- [7] S. Mintchev and D. Floreano, "Adaptive morphology: A design principle for multimodal and multifunctional robots," *IEEE Robot. Automat. Mag.*, vol. 23, no. 3, pp. 42–54, Sep. 2016.
- [8] R. D. Quinn et al., "Parallel complementary strategies for implementing biological principles into mobile robots," *Int. J. Robot. Res.*, vol. 22, pp. 169–186, 2003.
- [9] U. Saranli, M. Buehler, and D. Koditschek, "Rhex: A simple and highly mobile hexapod robot," *Int. J. Robot. Res.*, vol. 20, pp. 616–631, 2001.
- [10] C. Liu, O. Edwards, K. Althoefer, K. Zhang, and H. Godaba, "An electro-pneumatic shape morphing rolling robot with variable locomotion modes," in *Proc. IEEE 5th Int. Conf. Soft Robot.*, 2022, pp. 715–721.
- [11] Y.-S. Kim, G.-P. Jung, H. Kim, K.-J. Cho, and C.-N. Chu, "Wheel transformer: A wheel-leg hybrid robot with passive transformable wheels," *IEEE Trans. Robot.*, vol. 30, no. 6, pp. 1487–1498, Dec. 2014.
- [12] W. Xu, S. Wang, J. Fu, and P. Kang, "A morphing mobile robot with six-legged and spherical movement modes," in *Proc. IEEE Int. Conf. Inf. Automat.*, 2018, pp. 330–335.
- [13] T. F. Nygaard, C. P. Martin, J. Torresen, K. Glette, and D. Howard, "Real-world embodied AI through a morphologically adaptive quadruped robot," *Nature Mach. Intell.*, vol. 3, pp. 410–419, 2021.
- [14] M. Yim et al., "Modular self-reconfigurable robot systems [grand challenges of robotics]," *IEEE Robot. Automat. Mag.*, vol. 14, no. 1, pp. 43–52, Mar. 2007.
- [15] J. Germann, A. Maesani, R. Pericet-Camara, and D. Floreano, "Soft cells for programmable self-assembly of robotic modules," *Soft. Robot.*, vol. 1, pp. 239–245, 2014.
- [16] E. Hawkes et al., "Programmable matter by folding," *Proc. Nat. Acad. Sci.*, vol. 107, pp. 12441–12445, 2010.
- [17] M. A. Karimi, V. Alizadehyazdi, H. M. Jaeger, and M. Spencko, "A self-reconfigurable variable-stiffness soft robot based on boundary-constrained modular units," *IEEE Trans. Robot.*, vol. 38, no. 2, pp. 810–821, Apr. 2022.
- [18] L. Sun et al., "Stimulus-responsive shape memory materials: A review," *Mater. Des.*, vol. 33, pp. 577–640, 2012.
- [19] T. P. Chenal, J. C. Case, J. Paik, and R. K. Kramer, "Variable stiffness fabrics with embedded shape memory materials for wearable applications," in *Proc. IEEE/RSJ Int. Conf. Intell. Robots Syst.*, 2014, pp. 2827–2831.
- [20] M. Brancadoro, M. Manti, S. Tognarelli, and M. Cianchetti, "Fiber jamming transition as a stiffening mechanism for soft robotics," *Soft Robot.*, vol. 7, no. 6, pp. 663–674, 2020.
- [21] Y. Yang, Y. Zhang, Z. Kan, J. Zeng, and M. Y. Wang, "Hybrid jamming for bioinspired soft robotic fingers," *Soft Robot.*, vol. 7, no. 3, 2019.
- [22] A. Tonazzini, S. Mintchev, B. Schubert, B. Mazzolai, J. Shintake, and D. Floreano, "Variable stiffness fiber with self-healing capability," *Adv. Mater.*, vol. 28, pp. 10142–10148, 2016.
- [23] C. Liu, H. Qin, and P. T. Mather, "Review of progress in shape-memory polymers," *J. Mater. Chem.*, vol. 17, no. 16, pp. 1543–1558, 2007.
- [24] M. R. J. Scherer, *Double-Gyroid-Structured Functional Materials Synthesis and Applications*. Berlin, Germany: Springer, 2013.
- [25] A. Lipchitz, T. Imbert, and G. D. Harvel, "Investigation of fluid dynamic properties of liquid field's metal," in *Proc. ASME Power Conf.*, 2013, Art. no. V002T11A008.